


2023

## Effect of Ag2O nanosheets thickness on the performance of Al/GeO2/Ag2O/GeO2/C multifunctional electronic devices

Atef Fayez Qasrawi Prof. Dr.  
Arab American University - Jenin, atef.qasrawi@aaup.edu

Hazem Kh Khanfar Prof. Dr.  
Arab American University, Jenin, Hazem.khanfar@aaup.edu

Follow this and additional works at: <https://digitalcommons.aaru.edu.jo/aaup>

 Part of the [Physics Commons](#)

### Recommended Citation

Qasrawi, Atef Fayez Prof. Dr. and Khanfar, Hazem Kh Prof. Dr. (2023) "Effect of Ag2O nanosheets thickness on the performance of Al/GeO2/Ag2O/GeO2/C multifunctional electronic devices," *Journal of the Arab American University* مجلة الجامعة العربية الامريكية للبحوث: Vol. 9: Iss. 1, Article 1. Available at: <https://digitalcommons.aaru.edu.jo/aaup/vol9/iss1/1>

This Article is brought to you for free and open access by Arab Journals Platform. It has been accepted for inclusion in Journal of the Arab American University مجلة الجامعة العربية الامريكية للبحوث by an authorized editor. The journal is hosted on [Digital Commons](#), an Elsevier platform. For more information, please contact [rakan@aarj.edu.jo](mailto:rakan@aarj.edu.jo), [marah@aarj.edu.jo](mailto:marah@aarj.edu.jo), [u.murad@aarj.edu.jo](mailto:u.murad@aarj.edu.jo).

---

## Effect of Ag<sub>2</sub>O nanosheets thickness on the performance of Al/GeO<sub>2</sub>/Ag<sub>2</sub>O/ GeO<sub>2</sub>/C multifunctional electronic devices

### Cover Page Footnote

Copyright 2023, Journal of the Arab American University, All Rights Reserved.

# Effect of Ag<sub>2</sub>O nanosheets thickness on the performance of Al/GeO<sub>2</sub>/Ag<sub>2</sub>O/GeO<sub>2</sub>/C multifunctional electronic devices

Atef Qasrawi<sup>1\*</sup>, Hazem Khanfar<sup>2</sup>

<sup>1</sup>Department of physics, Arab American University, Jenin 240, Palestine,  
atef.qasrawi@aaup.edu

<sup>2</sup>Department of Telecommunications Engineering, Arab American University, Jenin 240,  
Palestine, hazem.khanfar@aaup.edu

## Abstract

Herein, stacked layers of germanium oxide comprising silver oxide nanosheets are used to fabricate multifunctional electronic devices. The performance of these devices is enhanced by altering the thickness of Ag<sub>2</sub>O nanosheets. The effect of *n* – Ag<sub>2</sub>O nanosheets on the electronic performance of stacked layers of *p* – GeO<sub>2</sub> is reported. The three stacked layers (GeO<sub>2</sub>/Ag<sub>2</sub>O/GeO<sub>2</sub>; named GAG) which are coated onto Al substrates under a vacuum pressure of 10<sup>-5</sup> mbar are subjected to measurements by X-ray diffraction, X-ray photoelectron, X-ray fluorescence, impedance spectroscopy, capacitance –voltage and current-voltage characteristics techniques. The impedance spectroscopy analysis indicates that altering the thickness of the Ag<sub>2</sub>O layer in the range of 25-75 nm could successfully engineer the operation ranges of the GAG devices. When operated as band pass/reject filters in the frequency domain of 0.01-1.80 GHz, the device shows the existence of three pass lines near and above 1.0 GHz. In addition, a controllable negative capacitance effect accompanied with resonance-antiresonance phenomena is observed in the studied frequency domains. On the other hand, investigations of the capacitance-voltage characteristics revealed metal-oxide-semiconductor-fields effect transistor characteristics displaying PMOS and NMOS channels under reverse and forward biasing conditions, respectively.

**Keywords:** GeO<sub>2</sub>/Ag<sub>2</sub>O/GeO<sub>2</sub>, MOSFET, nanosheets, enhanced filters, tunneling diode.

\* Corresponding author

## 1. Introduction

Germanium dioxide has attracted the attention of research society owing to its wide range of applications as a material suitable for the fabrication of electronic circuit components. They have been used in transient resistive switching memories (Feng et al., 2020). Resistive switching memories formed from layers of Ag/GeO<sub>2</sub>/fluorine-doped tin oxide are mentioned displaying resistance windows with a current “OFF/ON” ratios of 100. The devices showed a retention time of 10 h (Feng et al., 2020). As another kind of applications, Ge/GeO<sub>2</sub> interfaces are employed in Li<sup>+</sup> batteries (Yan et al., 2019). As lithium-ion battery anodes, they improved the capacity of the batteries allowing them to store 1.33 Ah/g at current density of 0.50 A/g (Yan et al., 2019). In addition, when used as waveguides, GeO<sub>2</sub> films displayed low attenuation level (0.1 dB/cm at 638 nm) in the spectral range that extends from visible light to near infrared (Khusayfan, Qasrawi, Alharbi, Khanfar, & Kayed, 2021). Such property makes the germanium dioxide films suitable for integrated photonics applications including dielectric waveguide materials. Moreover, SiO<sub>2</sub>/GeO<sub>2</sub> multilayers which are grown onto silicon substrates displayed metal-oxide-semiconductor (MOS) device characteristics (Antoja-Lleonart et al., 2020).

In general, multilayer stacks comprising nanosheets in its structure can perform as a multifunctional device based on its dielectric properties. For example, a barium titanate layer placed between the metal (Ag) thin film and the molybdenum disulphide layers remarkably enhanced the dielectric performance of these stacked layers when employed as biosensors (Almawgani et al., 2022). In addition, dielectric anisotropy realized by the optical ellipsometry technique on dielectric multi stacks indicated possible application of multi stacks based on light signal propagation direction (Taya & El-Agez, 2011). Nanosheets of Ag<sub>2</sub>O inserted between layers of GeO<sub>2</sub> remarkably increased the dielectric constant in the infrared range of light making GeO<sub>2</sub> ideal for device fabrication (Alharbi, Qasrawi, & Algarni, 2021). On the other hand, studies which take into account metal oxide doped GeO<sub>2</sub> reported information about the enhancement of the electrical performances of germanium dioxide as a result of preventing metal (doping agent)-Ge bond formation (Alharbi, Qasrawi & Algarni, 2021). This feature makes the GeO<sub>2</sub> more appropriate for high gate electronic applications (Lu et al., 2014). The metals (Al, Sc, Y), which are used as doping agents, played an important role in controlling the effective thickness of the oxide layers.

Based on these conclusions and on the important applications of germanium dioxide, here in this work, we are motivated to carry out a piece of work that targets enhancing the performance of germanium oxide- based devices. Particularly, by the insertion of silver oxide layers and altering their thicknesses, the electrical performances of Al/GeO<sub>2</sub>/C metal oxide semiconductor field effect transistors (MOSFET) is enhanced. In other words, the formed Al/GeO<sub>2</sub>/Ag<sub>2</sub>O/GeO<sub>2</sub> heterostructures will comprise Ag<sub>2</sub>O nanoslabs of thicknesses of 25 nm, 50 nm and 75 nm. The effect of the thickness of these nanosheets on structure of GeO<sub>2</sub>, on; the capacitance-voltage characteristics, current-voltage characteristics and on the capacitance, conductance, reflection coefficient, return loss and voltage standing wave ratios spectra in the frequency domain of 0.01-1.8 MHz will be explored. The class of applications of the germanium dioxide based MOSFET devices will be suggested (Yamamoto et al., 2011).

## 2. Experimental Details

Stacked layers of GeO<sub>2</sub> and Ag<sub>2</sub>O are prepared by the thermal evaporation technique using NORM VCM-600 thermal deposition system. During the evaporation cycles, the vacuum pressure was kept at 10<sup>-5</sup> mbar. The source materials were GeO<sub>2</sub> and Ag<sub>2</sub>O powders of high purity (99.99%, Alfa Aesar). The fabrication of the devices started by coating 500 nm thick layers of germanium dioxide onto ultrasonically and chemically cleaned Al films grown onto glass substrates by the thermal evaporation technique. In order to reveal the best characteristics of the proposed MOSFET devices, the thickness of the *n*-Ag<sub>2</sub>O is varied. Particularly, a *p*-GeO<sub>2</sub>/*n*-Ag<sub>2</sub>O/*p*-GeO<sub>2</sub> (GAG) fields effects transistors is composed of two 500 nm thick layers of germanium dioxide (regarded as semiconductor) sandwiched with silver oxide (accepted as oxide layer) nanosheets of thicknesses of 25, 50 and 75 nm are coated onto Al (metallic layer) substrates. GeO<sub>2</sub>/GeO<sub>2</sub> stacked layers comprising Ag<sub>2</sub>O of thicknesses of 25, 50 and 75 nm are named GAG-25, GAG-50 and GAG-75, respectively. The resulting Al/GeO<sub>2</sub>/Ag<sub>2</sub>O stacked layers were re-covered with another 500 nm thick third layer of GeO<sub>2</sub>. The top contacts were made by using high purity carbon paste. The area of the contact, which is presented by the schematics in the inset of Fig. 2 was  $7.82 \times 10^{-3} \text{ cm}^2$ . The thickness of the films was measured with the help of an in situ thickness monitor attached in the chamber of the thermal evaporator. It was also confirmed by profilometer. The produced films were characterized by the X-ray diffraction technique using Miniflex 600 XRD unit. The scanning speed of the XRD unit was 1°/min. The X-ray photoelectron spectroscopy measurements were handled with the help of XPS-ESCALAB 250).

The X-ray fluorescence spectroscopy (XRF) was measured with Rigaku ZSX Primus II XRF system. The conductivity type was tested by the hot probe technique. The current-voltage characteristics were recorded using Keithley I-V system equipped with programmable Keithley 230 voltage sources and Keithley 6285 Picoammeter. The impedance spectroscopy and capacitance-voltage characteristics were recorded with the help of Agilent 4291B impedance analyzer.

### 3. Results and discussion

#### 3.1 Design and energy band diagram

The main goal of this study was to discuss the possibility of formation of metal-oxide-semiconductor-field effect transistors (MOSFET) devices that could be employed as band pass/reject filters. The MOSFET device is designed from two oxide interfaces that forms *pn* heterojunction devices. For this purpose, wide and narrow bandgap semiconductors, namely *p*-GeO<sub>2</sub> and *n*-Ag<sub>2</sub>O, were selected. The theoretical energy band diagram of this system is shown in Fig. 1. The bands' bending after the oxides was stacked onto each other are shown by orange-colored lines (dashed orange lines show the bending in the vacuum level and solid orange line show band bending in valance and conduction bands). In accordance with the energy band diagram, the electron affinity ( $q\chi$ ), energy band gap ( $E_g$ ) and work function ( $q\phi$ ) values of GeO<sub>2</sub> were 2.24 eV (H. Kim et al., 2012), 5.30 eV and 7.58 eV (Madelung, 2012) (extrapolated from 5.03 eV (Miao, Yarbrow, Barton, & Seshadri, 2014), 1.20 eV and 5.30 eV (H. W. Kim, Na, Kwak, Cho, & Kwon, 2013), respectively. Stacking of these two layers led to a conduction band offset ( $\Delta E_c = |q\chi_{Ag_2O} - q\chi_{GeO_2}|$  (Ndikilar, Taura, Ejuh, & Muhammad, 2018)) of 2.79 eV. As the energy band gaps difference between the two stacked layers was  $\Delta E_g = |E_{g-GeO_2} - E_{g-Ag_2O}| = 4.10$  eV, a valance band offset of value of  $\Delta E_v = |\Delta E_g - \Delta E_c| = 1.31$  eV was expected before the band bending took place. The difference in the work function of both materials led to a built-in potential ( $qV_{bi} = |q\phi_{GeO_2} - q\phi_{Ag_2O}|$  (Ndikilar et al., 2018)) of 2.28 eV. After these two junctions were formed, the vacuum level of *n*-Ag<sub>2</sub>O bent down to achieve Fermi level ( $E_F$ ) equilibrium level. It is also important to notice that at the Al/*p*-GeO<sub>2</sub> side, as the work function of aluminum being 4.30 eV was less than the work function of *p*-GeO<sub>2</sub>, the Al/*p*-GeO<sub>2</sub> interfaces exhibited Schottky nature of contact. Since the work function of carbon was 5.10 eV, the same rule applied to C/*p*-GeO<sub>2</sub>. Thus, the currently reported device is of hybrid nature composed of two Schottky arms attached to a *pn* junction.

The built in potentials at the Schottky arms were  $qV_{bi} = |q\phi_{GeO_2} - q\phi_{Al,C}| = 3.28$  eV for the Al/p-GeO<sub>2</sub> and 2.48 eV for the C/p-GeO<sub>2</sub>. The high built in potential values indicates that the GAG devices are more appropriate for electric fields based passive mode devices (Ndikilar et al., 2018).

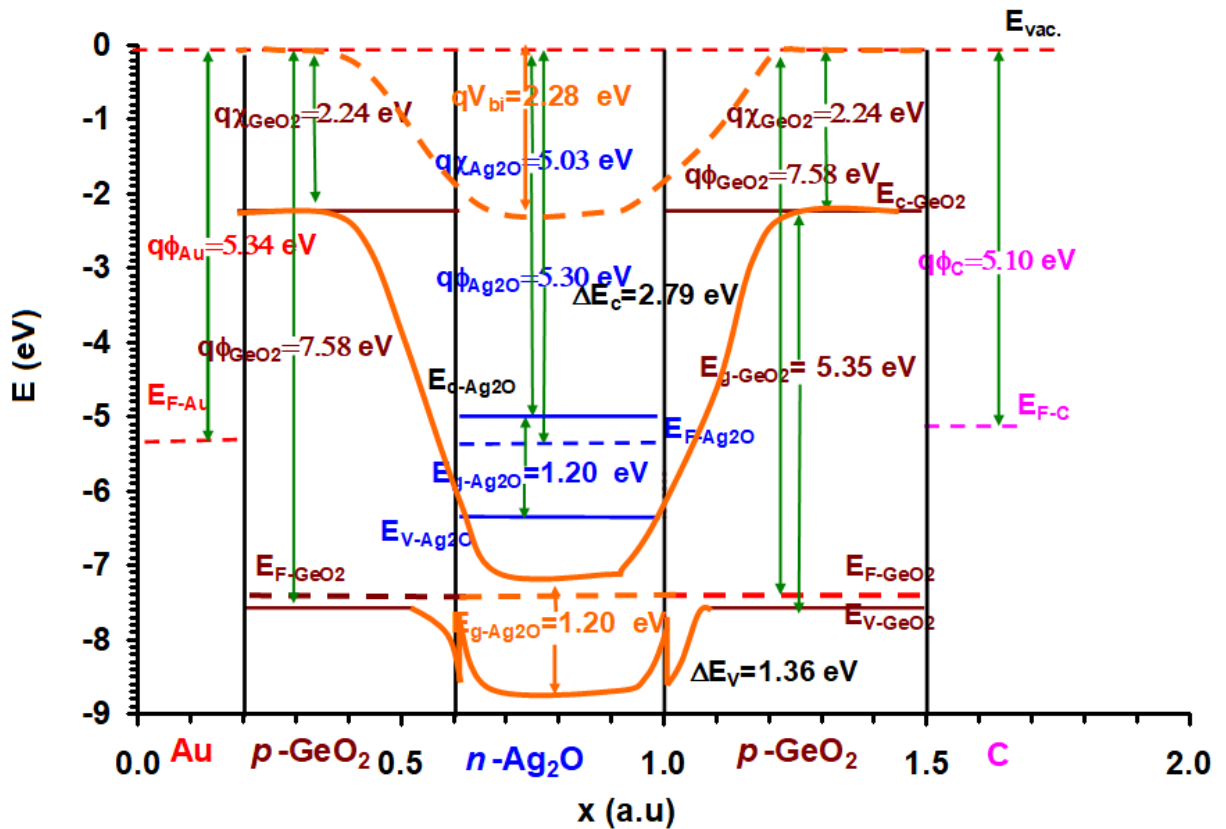


Figure 1: the energy band diagram for the GeO<sub>2</sub>/Ag<sub>2</sub>O/GeO<sub>2</sub> heterojunctions

Based on the above-mentioned energy band diagram, stacked layers of p-GeO<sub>2</sub> (semiconducting layers) comprising thin layers of Ag<sub>2</sub>O (oxide layers) were grown onto Al substrate and contacted with carbon point contact (metallic layers). While Ag<sub>2</sub>O was selected to prevent direct Ag-Ge bond formation, the carbon was selected because it forms strong bonds with semiconductor surfaces (Khusayfan, Qasrawi, & Khanfar, 2018a). The C/GeO<sub>2</sub> contacts are mentioned behaving as self-supporting film which can be used as binder-and collector-free anodes in flexible Li-ion batteries (Khusayfan et al., 2018a) (Pantò et al., 2017).

### 3.2 Structural analysis

The geometrical design and the X-ray diffraction patterns for the GAG devices are shown in Fig. 2. Analysis of the sharp peaks that appears in the figure indicated no diffraction patterns that could be assigned to germanium dioxide or silver oxide. It means that GeO<sub>2</sub> and Ag<sub>2</sub>O are both of amorphous structure. The stacked layers were also of amorphous nature in its as grown form. Except for the absence of the peaks of Al<sub>2</sub>O<sub>3</sub> in the GAG-75 samples, no remarkable effect of Ag<sub>2</sub>O nanoslabs on the structural properties of germanium oxide films was detected. When compared to the existing literature data, the apparent peaks were assigned to the cubic aluminum (3.977 Å) and hexagonal aluminum oxide ( $a = b = 4.7602 \text{ \AA}, c = 12.9933 \text{ \AA}, \alpha = \beta = 90^\circ, \gamma = 120^\circ$ ) (Fan, Ruiz-Hervias, Gurauskis, Sanchez-Herencia, & Baudín, 2016). The preferred interaction between the Al substrate and the condensing GeO<sub>2</sub> vapor during the growth cycle was assigned to the stronger bonding energy of Al-O(2) compared to Ge-O. It was mentioned that the bonding in GeO<sub>2</sub> was generated by Ge-O(1) and Ge-O(2) with bond lengths of 1.769 Å, 1.724 Å, respectively (Tsukada, Koide, Sasago, & Uchinokura, 1998). The bonding between Al and O atoms in Al<sub>2</sub>O<sub>3</sub> was also generated by Al-O (1) and Al-O(2) sites with bond lengths of 2.021 Å and 1.688 Å, respectively (Pan, Pu, & Jia, 2020). The bond length of Al-O (2) was shorter than the bond lengths of Ge-O(1) and Ge-O(2). Since the smaller the bond length, the higher the bond energy and stronger the bond is, the formation of Al<sub>2</sub>O<sub>3</sub> on the surface of the Al substrate is preferable (Sulaiman, Taura, Abdullahi Lawal, & Musa, 2019).

### 3.3 Surface stoichiometry and bulk composition

The surface stoichiometry of the top layer and the deep compositional analysis of the films were studied by the X-ray photoelectron (XPS) and X-ray fluorescence (XRF) spectroscopy techniques, respectively. Measurements of XRF spectra were made by exposing a beam power of 4 kW so that penetration of the stacked layers could be possible. For stacked layers of GAG-50 samples deposited onto Al substrates, all measurements of the stacked layers (Al, GeO<sub>2</sub>, Ag<sub>2</sub>O, GeO<sub>2</sub>) were evaluated. For a mass density of 0.138 mg/cm<sup>2</sup>, the oxide tests indicated the presence of Al<sub>2</sub>O<sub>3</sub>, GeO<sub>2</sub> and Ag<sub>2</sub>O with mass percentages of 45.3%, 20.0% and 34.7%, respectively. The analysis which took into account all the bulk of the films did not reveal any phases of GeO. When the elemental tests were carried out including Al substrates of total mass density of 0.138 mg/cm<sup>2</sup>, percentages of 29.7%, 24.0%, 13.9% and 32.4% were found relating to O, Al, Ge and Ag, respectively. No impurities were found in the films.



When the Al substrate was excluded from the calculations and the data was normalized to calculate the atomic contents, the samples were atomically composed of Ag<sub>2</sub>O and GeO<sub>2.18</sub>. The GeO<sub>2</sub> layers comprised ~ 3-4% excess oxygen. Previous studies, which targeted the stoichiometry analysis of GeO<sub>2</sub> thin films, concluded that during the growth cycle, because of the strong electronegativity of the second-nearest-neighbor oxygen atoms, partial decomposition of the GeO<sub>2</sub> source might cause sub-stoichiometry in the grown films. In this case, the sub-oxide might evolve into the Ge dioxide phase and the oxygen become excess (Ardayanian, Rinnert, Devaux, & Vergnat, 2006).

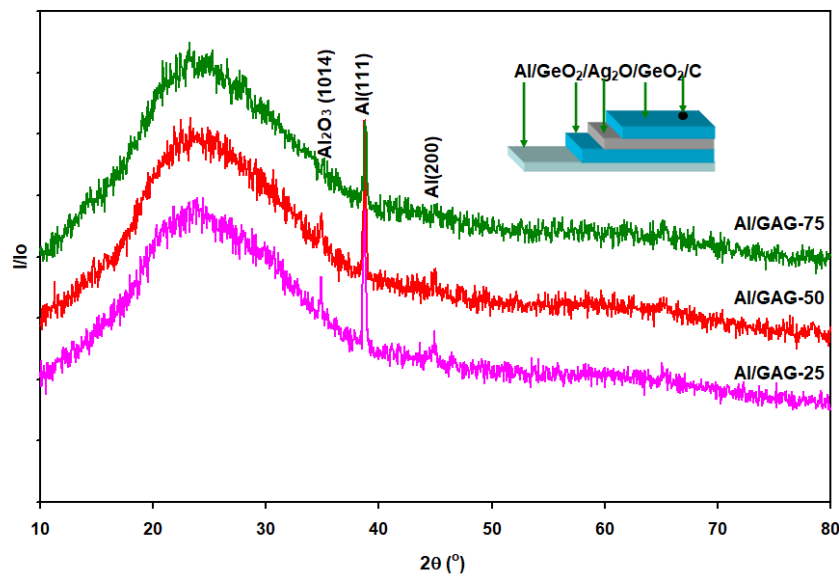


**Figure 2: The X-ray diffraction patterns for the stacked layers of GeO<sub>2</sub> comprising Ag<sub>2</sub>O nanosheets. The inset shows the geometrical design of the studied devices.**

On the other hand, Fig. 3 (a), (b) and (c) display the XPS spectra and the narrow scan of the peaks of Ge3d and O1s, respectively, for GAG-50 samples. As the XPS signal cannot exceed a depth of 10 nm, the integrated area under the assigned peaks indicates the possibility of determining the composition of the film at the top surface only. As appears in Fig. 3 (a), both peaks of Ge3d and O1s are present in the spectra assuring the formation of Ge-O bonds. The XPS signal included peaks of carbon. Carbon is captured from the surrounding.

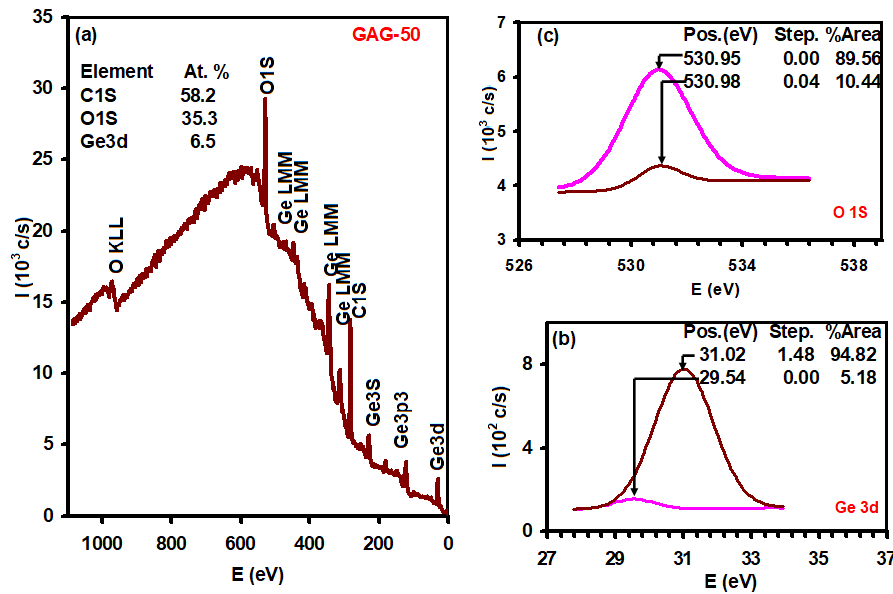


**Figure 3: (a) the X-ray photoelectron spectra for GAG -50 samples. (b) and (c) are the binding energy spectra for Ge3d and O1S, respectively.**

In addition, the XPS spectra of O1S (Fig. 3(c)) show a hardly distinguishable two- band structure. The peak centered at 530.98 eV is characteristic of metallic oxides and the other dominant peak centered at 530.95 eV is assigned to different surfaces oxidized hydrocarbon (contamination) (Wang et al., 2019). The peak of Ge3d which is centered at ~29.2 eV is also composed of two-band structure (Fig. 3 (b)). The dominant peak centered at 31.02 eV is assigned to GeO while the other peak observed at 29.54 eV is attributed to Ge element (Beynon, El-Samanoudy, & Short, 1988). The data suggests that because of the interaction with carbon on the surface, a non-stoichiometric composition is established at the surface of the film. Namely, GeO<sub>2</sub> decomposes to GeO<sub>x</sub> and Ge. Literature data on XPS signals of GeO<sub>2</sub> reported that GeO<sub>2</sub> exhibits defective structure with compositional formula of GeO<sub>1.75</sub> instead of GeO<sub>2</sub> (Beynon et al., 1988). Our XPS quantitative calculations revealed the formation of GeO<sub>0.60</sub>. The content of the 10 nm thick surface is composed of 59.97% GeO<sub>0.60</sub> and 40.03% Ge. Recent reports mentioned that amorphous germanium clusters are formed due to the chemical reaction between substrate and germanium oxide layers. As GeO<sub>x</sub> is not stable, during the growth cycle, it decomposes into germanium and germanium dioxide (Gambaryan et al., 2020).

### 3.4 Microwave resonating and filtering

The first test that targeted proofing the applicability of the constructed Al/GAG-xx/C devices as band filters was the measurement of the capacitance ( $C$ ) and the conductance ( $G$ ) spectra in the frequency domain of 0.01-1.80 GHz. The test results are shown in Fig. 4 (a) and (b), respectively. It is clear from Fig. 4 (a) that the capacitance spectra exhibit resonance-antiresonance phenomena followed by negative capacitance (NC) effect. The resonance peaks are observed at 0.81 GHz, 0.46 GHz and at 0.51 GHz, for the GAG-25, GAG-50 and GAG-75, devices respectively. Increasing the thickness of Ag<sub>2</sub>O slabs from 25 nm to 50 nm shifts the resonance peaks toward lower frequency range. Raising the slabs thickness to 75 nm slightly shifts the peak to a larger value. It is also noticeable that the thicker the nanoslabs, the sharper the resonance peak and the larger the positive capacitance value. Namely, the resonance peaks exhibit maxima of 3.6 nF, 11.1 nF and 38.1 nF as the Ag<sub>2</sub>O layer thickness increases from 25 nm to 50 nm and reaches 75 nm, respectively. On the other hand, the conductance spectra which appear in Fig. 4 (b) display one shoulder followed by one absolute and two local maxima. While the  $G - f$  shoulder appears at 0.20 GHz and not affected by the  $p$ -layer thickness (Ag<sub>2</sub>O nanosheets), the maximum and one of the local conductance peaks are shifted from 0.78 GHz, to 0.43 GHz and to 0.50 GHz and from 1.13 GHz to 1.27 GHz and to 1.31 GHz, as the  $p$ -layer thickness increases from 25 nm to 50 nm and reaches 75 nm, respectively. The other local peak which is detected at 1.48 GHz is not shifted but its value decreased with increasing  $p$ -layer thickness. In relation to the X-ray diffraction results, the largest positive capacitance and highest absolute conductance are pronounced in the samples where the peaks of aluminum oxide are absent. For GAG-50 and GAG-75 samples, the thicker the Ag<sub>2</sub>O nanoslabs, the larger the conductance. Al<sub>2</sub>O<sub>3</sub> is known to exhibit very high electrical resistivity values ( $10^{12} \Omega cm$ ) (Shi, Cho, Goto, & Sekino, 2020). This value is  $10^7$  times larger than that of Ag<sub>2</sub>O ( $5 \times 10^5 \Omega cm$ ) (ISMAL, YAHYA, & ABDULRAZAQ, 2005). Thus, increasing the Ag<sub>2</sub>O contents by increasing the slabs thicknesses increases the holes concentration leading to a more conductive heterojunction device. In general, regions where the conductivity shows peak-like variation are mostly dominated by two conduction mechanisms, namely by the quantum mechanical tunneling (QMT) and the correlated barriers hopping (CBH). These types of current conduction mechanisms are famous in heterojunction devices like CdS/Sb<sub>2</sub>Te<sub>3</sub> tunneling diodes (Khusayfan, Qasrawi, & Khanfar, 2018b), Cu<sub>2</sub>O/ZnO (Li et al., 2013), Al/MoO<sub>3</sub>/ZnPc/Al broken gap tunneling hybrid devices (Qasrawi & Khanfar, 2020) and Ga<sub>2</sub>S<sub>3</sub>-Ga<sub>2</sub>Se<sub>3</sub> films (Bekheet, 2008).

The signs of the domination of the QMT were explored by the observation of the variation of the exponent ( $s$ ) of the  $\sigma = Aw^s$  of the conductivity ( $\sigma = Gl/A$ ;  $l$  is device thickness and  $A$  is the point contact area)- angular frequency ( $w = 2\pi f$ ) dependencies (Khusayfan et al., 2018b). For the QMT to dominate  $s$  should be decreasing with increasing  $f$ . The execution of the derivative,  $s = d\ln(G)/d\ln(f)$ , which is shown in the inset of Fig. 4 (a) ended with the result that  $s$  decreases with increasing  $f$  value in the range of  $\sim 0.02$ - $0.17$  GHz. For larger frequency values,  $s$  starts increasing with increasing signal frequency. In that range the domination of the CBH is more pronounced.

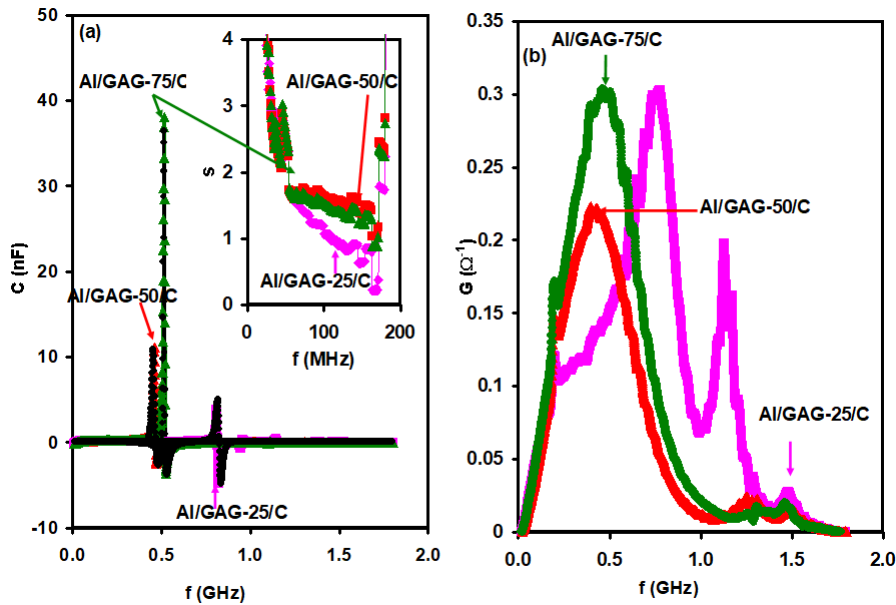


**Figure 4:** (a) the capacitance and (b) the conductance spectra for Al/GeO<sub>2</sub>/Ag<sub>2</sub>O/GeO<sub>2</sub>/C devices. The inset of (a) show the variation of the exponent  $s$  of the equation,  $G \propto F^s$ . The black colored circles in (a) represent the fitting of Eqn. (1).

On the other hand, the resonance –antiresonance phenomenon, which is observed in the capacitance spectra is theoretically reproduced assuming the validity of the modified Qasrawi-Ershov model (Qasrawi & Khanfar, 2020) (Bekheet, 2008) (Ershov et al., 1998). The model fits the negative capacitance and resonance in capacitance spectra. In that model, the capacitance is composed of geometrical ( $C_o$ ) and dynamic parts ( $C_1$ ). The dynamical capacitance is dominated by two charging processes one for  $p$  –type dielectric media and another for  $n$  –type. Since the dynamical capacitance is representative of the effective dielectric constant, it follows the same type of variations like that of the dielectric dispersion. Particularly, resonance in dielectric spectra is observed at signal angular frequencies ( $w$ ) equal to the plasmon frequency ( $w_{n,p}$ ).

Formation of hole-plasmon and electron-plasmon in accordance with the Drude approach for dielectric dispersion give dielectric media the chance to exhibit negative dielectric constant characteristics. The total capacitance spectra can then be presented by the form (Qasrawi & Khanfar, 2020) (Bekheet, 2008) (Ershov et al., 1998),

$$C(w) = C_o + C_1 = C_o + \left( \frac{a_n \tau_n}{1+(w-w_n)^2 \tau_n^2} - \frac{a_p \tau_p}{1+(w-w_p)^2 \tau_p^2} \right). (1)$$

In this equation,  $a_n, a_p, \tau_n, \tau_p$  and  $w_n, w_p$  are the rate of change of capacitance with time in F/s, the relaxation time or scattering time and the plasmon frequencies for electrons cloud and for holes cloud, respectively. The reproduced capacitance spectra for the studied samples are shown by black solid circles in Fig. 4 (a). The good agreement between theory and experiments was achieved with the fitting parameters which are shown in Table 1. As the table shows no effect of Ag<sub>2</sub>O thickness on the  $C_o, a_n$  and  $a_p$  values is observed. However, while the scattering (relaxation) time increases with increasing  $n$ -layer thickness, the plasmon frequency of electrons shifts toward lower values. The plasmon frequency depends on the square root of the free charge carrier density (Dresselhaus, 2001). Thus, the decrease in the plasmon frequency is attributed to the participation of freer electrons associated with increased thickness of the  $n$ -type layers. The electrons recombine with holes at the  $pn$  interfaces leading to a decrease in the number of free holes generated from  $p$ -GeO<sub>2</sub> layers. The reduction in the free holes density accounts for the shift in the resonance peak of the capacitance spectra toward lower frequency values. In addition, the scattering time which increases with increasing Ag<sub>2</sub>O nanoslabs thickness provides information about the electronic friction coefficient in the GAG heterojunction devices. The friction coefficient ( $\gamma \propto \tau_{n,p}^{-1}$ ) for electrons motions decreases with increasing  $n$ -layers thickness while that of holes increase as the Ag<sub>2</sub>O nanoslabs thickness is increased from 25 to 50 nm.

**Table 1: The fitting parameters for the capacitance spectra of Al/GeO<sub>2</sub>/Ag<sub>2</sub>O/GeO<sub>2</sub>/C devices**

parameter	Al/GAG-25/C	Al/GAG-50/C	Al/GAG-75/C
$C_o$ (pF)	100	100	100
$a_n$ (F/s)	1.00	1.00	1.00
$a_p$ (F/s)	1.00	1.00	1.00
$w_n$ (GHz)	5.15	2.85	3.22
$w_p$ (GHz)	5.22	2.95	3.25
$\tau_n$ (ns)	11	15	44
$\tau_p$ (ns)	11	5	8
$V_{bi-p}/V_{bi-n}$ (eV)	8.77/8.51	3.35/2.06	3.80/3.21
$N_a, N_d$ ( $\times 10^{18} \text{ cm}^{-3}$ )	1.60/1.56	1.02/0.62	0.58/0.49
$w_{Dp}, w_{Dn}$ (nm)	35/35	27/27	38/38

In addition to the electron/hole-plasmonic interactions, which are discussed here, other reasons that account for the negative capacitance effect could be the minority carrier injection caused by accumulation of minority carriers at the interfaces (Ershov et al., 1998). The charge polarization effect (polarization versus electric field) could also be reason for the NC effect observed in our heterojunction devices (Çavdar, Koralay, Tuğluoğlu, & Günen, 2005). Regarding the thin film transistors, they are believed to originate from the depolarization field which produces a decreasing voltage across the field effect capacitance while the induced charge is increasing (Zhou et al., 2019). Stacked layers of selenium containing Ag nanosheets exhibited negative capacitance effect as a result of increased strain and defect densities (Qasrawi & Aloushi, 2019).

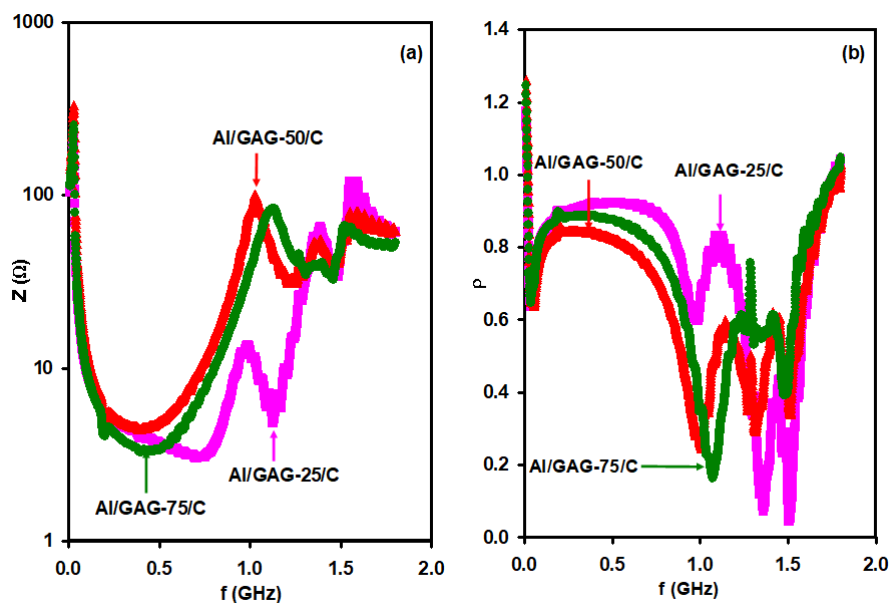


**Figure 5: (a) the impedance and (b) the reflection coefficient spectra for Al/GeO<sub>2</sub>/Ag<sub>2</sub>O/GeO<sub>2</sub>/C devices.**

Fig. 5 (a) shows the impedance spectra ( $Z$ ) of the devices under study. The impedance values sharply decrease from 331.2  $\Omega$  at 0.01 GHz to  $\sim$ 5.85  $\Omega$  at 0.17 GHz. Regardless of the  $n$  –layers thickness the impedance is the same and exhibit the same value and the same trend of variation. This region is the frequency domain where the quantum mechanical tunneling conduction process was dominant. In the range of 0.17-1.80 GHz, the impedance spectra display peaks at 0.99 GHz, 1.40 GHz and at 1.55 GHz for the devices comprising 25 nm Ag<sub>2</sub>O slabs in its structure. For the GAG-50 and GAG-75 devices the peaks appear at 1.04 GHz, 1.37 GHz and 1.55 GHz and at 1.14 GHz, 1.41 GHz and at 1.54 GHz, respectively. The impedance values for the GAG-50 and for the GAG-75 devices are higher than that of GAG-25. On the other hand, Fig. 5 (b) shows the magnitude of the reflection coefficient spectra

$$(\rho = \left| \frac{Z_{Source} - Z_{GAG-xx}}{Z_{Source} + Z_{GAG-xx}} \right|)$$
 (Poazar, 2011) (Chaturvedi, 2018)). The reflection coefficient provides information about the applicability of the devices as band pass/reject filters. Values of  $\rho = 0$  indicate perfect matches between sources and device. In this case, the device behaves as bands pass filter. All propagating signals pass without attenuation. Values of  $\rho = 1.0$  indicate bands reject filter characteristics in which all incident signals are rejected. For our devices, it is clear from Fig. 5 (b) that three notch frequencies ( $f_{cn}$ ) do exist in each device. Namely, they are  $f_{c1}$ ,  $f_{c2}$  and  $f_{c3}$  centered at 0.99 GHz, 1.36 GHz and 1.52 GHz, respectively. The thickness of the Ag<sub>2</sub>O slabs strongly affects the value of  $\rho$  and slightly shifts the value of  $f_{cn}$ . As it is clear from the figure, at  $f_{c1}$ , the reflection coefficient decreases from 0.60 to 0.26 and reaches 0.17 as the Ag<sub>2</sub>O nanoslabs thickness increases from 25 nm to 50 nm and reaches 75 nm, respectively. For these samples,  $f_{c1}$  also shift from 0.99 GHz to 1.01 GHz and reach 1.08 GHz.  $\rho$  values increase from 0.08 to 0.30 and reaches 0.55 at  $f_{c2}$  and increases from 0.047 to 0.35 and reaches 0.41 at  $f_{c3}$  as the Ag<sub>2</sub>O nanoslabs thickness increases from 25 nm to 50 nm and reaches 75 nm, respectively. It is evident from these values that while the GAG-25 devices are more effective as band filters in the gigahertz range of frequency, GAG-50 and GAG-75 samples are more appropriate for megahertz frequency domain. The quality of these multiband pass/reject filters is readable from the return loss ( $L_r = -20 \log(\rho)$ ) (Poazar, 2011) (Chaturvedi, 2018)) and voltage standing wave ratios ( $VSWR = \frac{1+\rho}{1-\rho}$ ) spectra which are shown in Fig. 6 (a) and (b), respectively. In general, excellent impedance matches between sources and device needs return loss values larger than 20 dB. This value is reached at  $f_{c2}$  and  $f_{c3}$  for the Al/GeO<sub>2</sub>/Ag<sub>2</sub>O/GeO<sub>2</sub>/C devices having Ag<sub>2</sub>O nanoslabs of thicknesses of 25 nm in its structure. The other two devices display good  $L_r$  values at  $f_{c1}$  only. The  $VSWR$  spectra which appear in Fig. 6 (b) display values close to 1.0 at  $f_{c1}$  for the GAG-50 and GAG-75 samples and at  $f_{c2}$  and  $f_{c3}$  for the GAG-25 samples. The  $VSWR$  provides information about the peak voltage that can be found on a line under non-ideal match conditions. It is also a common measure of the “goodness” of a match. A perfect match is characterized by a  $VSWR$  of 1 (Poazar, 2011) (Chaturvedi, 2018), while a short or open circuits produces a  $VSWR$  of infinity. The performance of the GAG-xx devices as band pass/reject filters is highly compatible with the recent developments in that sector (Chaturvedi, 2018).

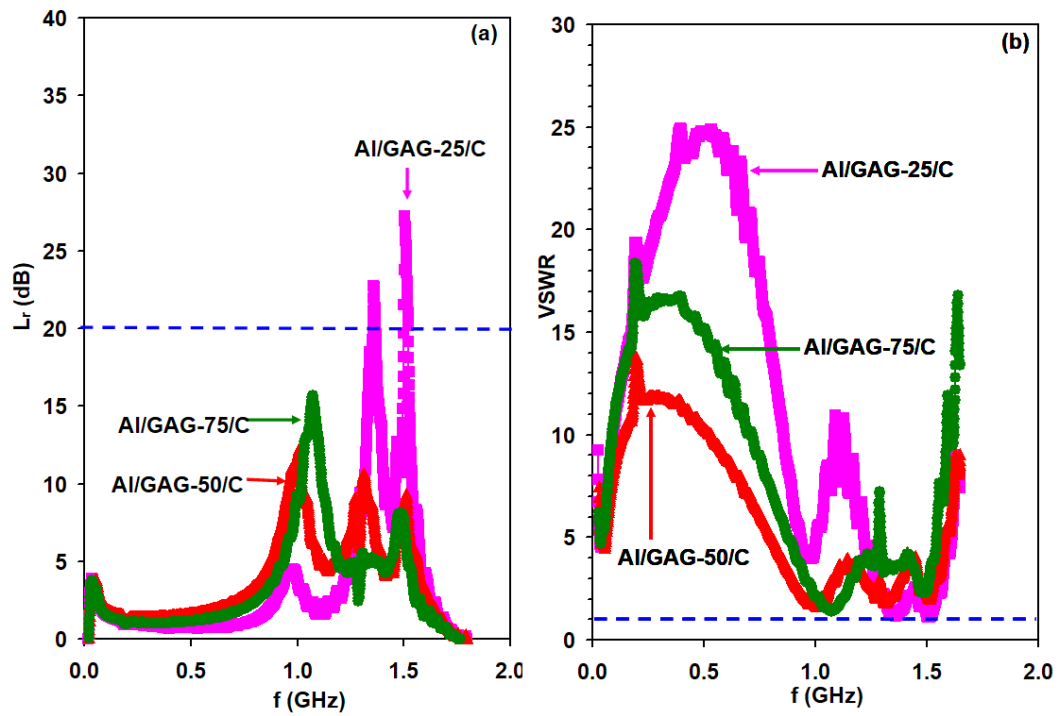


Figure 6: (a) the return loss spectra and (b) the voltage standing wave ratios for the Al/GeO<sub>2</sub>/Ag<sub>2</sub>O/GeO<sub>2</sub>/C devices.



### 3.5 MOSFET device characteristics

As a main target of the work that aimed at finding another kind of application for the Al/GeO<sub>2</sub>/Ag<sub>2</sub>O/GeO<sub>2</sub>/C devices, the capacitance -voltage and current (*I*)-voltage characteristics for the samples were recorded at room temperature. For GAG-25, GAG-50 and GAG-75 devices, the capacitance displayed negative capacitance values in the frequency domain of 1.0-2.5 MHz. Thus, the *C* – *V* characteristics were studied above 3.0 MHz to obtain positive capacitance values. The positive *C* – *V* characteristics provide information about the depletion region of capacitance. Illustrative *C* – *V* characteristics for the GAG-50 sample is shown in Fig. 7 (a). The figure displays typical MOSFET (metal oxide semiconductor field effects transistor) characteristics in which an inversion mode of PMOS transistor appears under reverse biasing conditions and an inverted mode of operation of NMOS characteristics dominates under forward biasing conditions (Pintilie, Stancu, Trupina, & Pintilie, 2010) (Sze & Ng, 2006). In the PMOS mode of operation, when activated by lowering the voltage below ~ 0.50 V, the device allows the conduction of holes reaching a minimum capacitance value at  $V = -0.08 V$ . As the applied voltage become positive, the NMOS appears as an inversion layer in the GeO<sub>2</sub> (*p*- layer) forming *n* – channel. Conduction in this channel is dominated by electrons. This behavior is assigned to the charge dynamics. As appears in Fig. 7 (b), re-plotting the recorded capacitance-voltage characteristics in accordance with depletion region equation (Sze & Ng, 2006),

$$C^{-2} = 2(V - V_{bi} - \frac{kT}{q}) / (qA^2\epsilon_s N), \quad (2)$$

The built in potential ( $qV_{bi}$ ), the donor ( $N_d$ ) or acceptor ( $N_a$ ) concentrations and the depletion region widths ( $w_{Dn} = \sqrt{2 \epsilon_s V_{bi} / (qN_d)}$ ,  $w_{Dp} = \sqrt{2 \epsilon_s V_{bi} / (qN_a)}$ ) in the *n* and *p*-channels, respectively, are calculated. In the above equations, *q* is the electron charge, *A* is the area of the device and  $\epsilon_s$  is the high frequency effective dielectric constant of the stacked layers. The value of the high frequency dielectric constants for GeO<sub>2</sub> and Ag<sub>2</sub>O are taken as 4.1 (Madelung, 2012) and 4.0 (Gao et al., 2010), respectively. With these values the dielectric constant,  $\epsilon_s = (\epsilon_{GeO_2}^{-1} + \epsilon_{Ag_2O}^{-1})^{-1}$  of the *pn* layers is 2.02. The linear plots of the  $C^{-2} - V$  variations allowed determining the MOSFET device parameters ( $qV_{bi}, N_a, N_d, w_{Dn}, w_{Dp}$ ). The device parameters are listed in Table 1. In accordance with the table, the built in potential for the device is strongly affected by the thickness of the Ag<sub>2</sub>O layer.

Theoretically, the highest possible built in potential value being 10.11 eV is that resulting from the addition of the potential at the Al/GeO<sub>2</sub> ( $qV_{bi} = 3.35 \text{ eV}$ ), GeO<sub>2</sub>/Ag<sub>2</sub>O ( $qV_{bi} = 2.28 \text{ eV}$ ) repeated two times and at Au/GeO<sub>2</sub> ( $qV_{bi} = 2.24 \text{ eV}$ ). The calculated data suggest a depletion width of 35 nm. This value is thicker than the coated Ag<sub>2</sub>O layers. In this case, the whole Ag<sub>2</sub>O film is depleted. Increasing the thickness of the Ag<sub>2</sub>O layer to 50 nm remarkably decreased the built in potential values to 3.35 eV at the PMOS side and to 2.06 eV at the NMOS side. Increasing the Ag<sub>2</sub>O layer further increases the built in potential values. In addition, it is observed that with the increase in the thickness of the  $n$  –layer from 25 nm to 75 nm, both of the donors and acceptors concentrations decreases. Studies on MOSFET devices exhibiting a lowering in the carrier concentrations as a result of increased thickness assigned this behavior to the accumulation of electrons and holes at heterojunction interface in two-dimensional fashion (Esaki, 1984). When the thickness of the Ag<sub>2</sub>O layer is sufficiently increased, the MOSFET devices can be regarded as a series of isolated heterojunctions. In this case, most electronic conduction takes place at heterojunction interfaces forcing the electrons and holes to accumulate in a two-dimensional fashion leading to the observed decrement in donor/acceptor concentrations (Esaki, 1984).

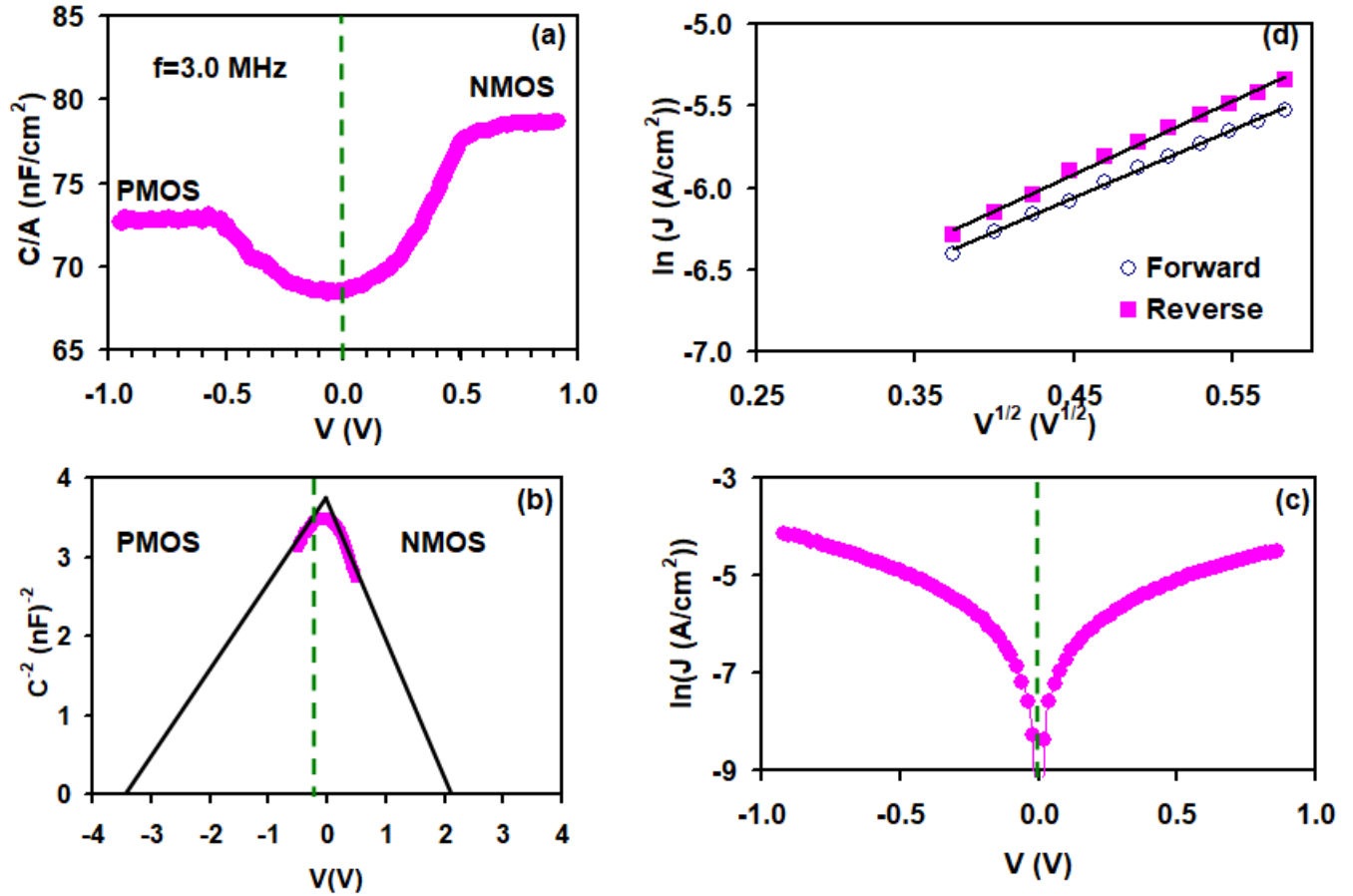


Figure 7: (a) the capacitance-voltage characteristics, (b) the  $C^{-2} - V$  variations, (c) the current-voltage characteristics and (d) the  $\ln(I) - \sqrt{V}$  variations for Al/GeO<sub>2</sub>/Ag<sub>2</sub>O/GeO<sub>2</sub>/C devices.

### 3.6 Tunneling diode characteristics

Fig. 7 (c) displays a representative curve of the current ( $I$ ) density ( $J = \frac{I}{A}$ ;  $A = 7.85 \times 10^{-3} \text{ cm}^2$ ) -voltage ( $V$ ) characteristics for one of the devices under study. Namely, for the GAG-50 device, the  $J - V$  curves display high current values under forward and reverse biasing conditions. The large reverse current values appear when the positive electrode is Aluminum. Attempts to explore the current conduction mechanisms in the samples included plotting of  $\ln(J) - V$  characteristic curves in accordance with the Schottky Richardson equation (Sze & Ng, 2006). This current conduction mechanism relates to conduction by thermionic emission ( $I = AA^*T^2 e^{-\frac{q\phi}{kT}} (e^{qV/nkT} - 1)$ ,  $A^*$ ,  $T$ ,  $\phi$  and  $n$  are Richardson constant, temperature, barrier height and ideality factor respectively) (Sze & Ng, 2006). However, plots of  $\ln(J) - V$  did not show linear regions with

high coefficient of determination ( $R^2$ ). The highest coefficient of determination values ( $R^2 > 0.99$ ) was achieved for the plots of  $\ln(J) - \sqrt{V}$  variations which are shown in Fig. 7 (d). The linear plots of the  $\ln(J) - \sqrt{V}$  variations in accordance with the equation,  $J = I/A = A^*T^2 e^{q(-\phi + a\sqrt{\frac{V}{wDn}})}$  (Qasrawi, 2014) indicate the domination of charge transport by direct tunneling (low voltage) process of Schottky emission type (Govor, Reiter, & Parisi, 2016). The same current conduction mechanism is observed for the GAG-25 and GAG-75 samples (not shown). In accordance with the plots of the  $\ln(J) - \sqrt{V}$  variations (Fig. 7 (d)), the linear slopes allow determining the width of the tunneling barrier in which the current pass through. The calculated tunneling barrier height and width in the presented sample (GAG-50) is found to be 0.61 eV and 0.61 eV, and 61nm and 53 nm under forward and reverse biasing conditions, respectively. Repeated calculations for GAG-75, revealed barrier heights of 0.62 and 0.53 eV and barrier widths of 63 and 57 nm, under forward and reverse conditions, respectively. Compared to the values listed in Table 1, the barrier width which is determined from  $\ln(J) - \sqrt{V}$  variations are, approximately, two times larger. This is just because under low electric fields, the tunneling barrier width is strongly influenced by the energy barrier between the  $n$ - and  $p$ -channels and by the recombination dynamics at the interfaces (Roh et al., 2014). The domination of the tunneling current conduction mechanism which was also observed in the conductance spectra below 0.17 GHz, limits the rectifying properties of the MOSFET devices. It leads to the domination of high reverse currents. In general, in heterojunction devices, the large reverse current is often inevitable as the reverse tunneling current is significant in thin  $p$ - $n$  junctions (Wu et al., 2019). The large reverse biased leakage currents could also be assigned to the generation-recombination via mid-band traps assisted by the Frenkel-Poole emission of carriers from these traps (Hasbullah, David, & Mowbray, 2011). As a macroscopic look at the overall of the analysis, it is possible to guess from the X-ray diffraction and X-ray photoelectron spectral technique, that the amorphous nature of the films leads to high degree of disorder. The surface of the devices is strongly influenced by the surrounding that strongly interacts with carbon forcing oxygen deficiency. This in turn results in excess amount of unreacted germanium which also behave as surface traps. On the other hand, the XRF analysis which allow deep investigations through bulk have shown the presence of excess oxygen.

Studies on the role of excess oxygen on the electrical properties of materials have shown that the excess oxygen forms conducting channels and increases the electrical conductivity (Banerjee, Ghosh, & Chattopadhyay, 2005). Consistently, literature data mentioned that Presence of negative capacitance is due to the accumulation of ions at the metal/semiconductor interface. Accumulation of ions is facilitated by excess oxygen, vacancies and interface charge states in gallium doped zinc oxide (Girija, Somasundaram, Debnath, Topkar, & Vatsa, 2018). Studies on Hf based oxides have shown that excess oxygen can form oxygen interstitial defects; these defects relate to hole conduction in a PMOS device leading to an enhanced MOSFET characteristics (Jo et al., 2008). In layers of HfSiO, the excess oxygen caused generation of holes trapping sites (Jo et al., 2008). The interaction between excess Ge at the surface and excess oxygen in the bulk could be a one significant reason for observed resonance –antiresonance phenomena in GAG-xx devices.

#### 4. Conclusions

Here, in this study, we aimed to fabricate multifunctional devices based on germanium oxide. The performance of these devices was improved by the insertion of *n* –type Ag<sub>2</sub>O nanosheets between stacked layers of GeO<sub>2</sub>. Using standard measuring techniques, we have shown the possibility of engineering a multifunctional GeO<sub>2</sub> based electronic devices via increasing the thickness of the *n* –Ag<sub>2</sub>O layer which is sandwiched between two *p* –GeO<sub>2</sub> layers. The fabricated electronic devices exhibited negative capacitance effect, band pass/reject filter characteristics, metal oxide fields effect transistor (MOSFET) and tunneling diode characteristics. The tests on this multifunctional device nominate it for use as microwave resonators with three notch frequencies. In general, from technological point of view, with NC effect, resonance-antiresonance, tunneling effect and other properties, the devices can be employed as amplifiers, parasitic capacitance cancelers, noise reducers, microwave band filters and MOSFET devices.

## References

1. Alharbi, S. R., Qasrawi, A. F., & Algarni, S. E., (2021). Effects of Ag<sub>2</sub>O nanosheets, on the structural, optical and dielectric properties of GeO<sub>2</sub> stacked layers. *Physica Status Solidi B*, 258 (5), 2000578.
2. Almawgani, A.H., Taya, S.A., Daher, M.G., Colak, I., Wu, F. and Patel, S.K., 2022. Detection of glucose concentration using a surface plasmon resonance biosensor based on barium titanate layers and molybdenum disulphide sheets. *Physica Scripta*, 97(6), p.065501.
3. Antoja-Lleonart, J., Zhou, S., Hond, K. d., Huang, S., Koster, G., Rijnders, G., & Noheda, B. (2020). Atomic layer deposition of SiO<sub>2</sub>-GeO<sub>2</sub> multilayers. *Applied Physics Letters*, 117(4), 041601.
4. Ardyanian, M., Rinnert, H., Devaux, X., & Vergnat, M. (2006). Structure and photoluminescence properties of evaporated GeO<sub>x</sub> thin films. *Applied Physics Letters*, 89(1), 011902.
5. Banerjee, A. N., Ghosh, C. K., & Chattopadhyay, K. K. (2005). Effect of excess oxygen on the electrical properties of transparent p-type conducting CuAlO<sub>2+x</sub> thin films. *Solar Energy Materials and Solar Cells*, 89(1), 75-83.
6. Bekheet, A. E. (2008). Ac conductivity and dielectric properties of Ga<sub>2</sub>S<sub>3</sub>-Ga<sub>2</sub>Se<sub>3</sub> films. *Physica B: Condensed Matter*, 403(23), 4342-4346.
7. Beynon, J., El-Samanoudy, M.M. and Short, E.L., 1988. Evaluation of the composition of reactively evaporated GeO<sub>x</sub> thin films from optical transmission and XPS data. *Journal of materials science*, 23(12), pp.4363-4368.
8. Çavdar, Ş., Koralay, H., Tuğluoğlu, N., & Günen, A. (2005). Frequency-dependent dielectric characteristics of Tl-Ba-Ca-Cu-O bulk superconductor. *Superconductor Science and Technology*, 18(9), 1204-1209.
9. Chaturvedi, P. K. (2018). Simple Laboratory Experiments and Laboratory Manual *Microwave, Radar & RF Engineering* (pp. 423-466): Springer.
10. Dresselhaus, M.S., 2001. Transport Properties of Solids. *Lecture Notes. In:-Solid State Physics-Part 1*.

11. Ershov, M., Liu, H. C., Li, L., Buchanan, M., Wasilewski, Z. R., & Jonscher, A. K. (1998). Negative capacitance effect in semiconductor devices. *IEEE Transactions on Electron Devices*, 45(10), 2196-2206.
12. Esaki, L., 1984. Advances in semiconductor superlattices, quantum wells and heterostructures. *Le Journal de Physique Colloques*, 45(C5), C5-3.
13. Fan, K., Ruiz-Hervias, J., Gorauskis, J., Sanchez-Herencia, A. J., & Baudín, C. (2016). Neutron diffraction residual stress analysis of Al<sub>2</sub>O<sub>3</sub>/Y-TZP ceramic composites. *Boletín de la Sociedad Española de Cerámica y Vidrio*, 55(1), 13-23.
14. Feng, J., Hu, W., Zeng, F., Lin, H., Li, L., Yang, B., Peng, Y., Wu, D., Huo, B. and Tang, X., 2020. Investigation of physically transient resistive switching memory based on GeO<sub>2</sub> thin films. *Applied Physics Letters*, 117(19), 192102.
15. Gambaryan, M. P., Krivyakin, G. K., Cherkova, S. G., Stoffel, M., Rinnert, H., Vergnat, M., & Volodin, V. A. (2020). Quantum Size Effects in Germanium Nanocrystals and Amorphous Nanoclusters in GeSixOy Films. *Physics of the Solid State*, 62(3), 492-498.
16. Gao, X.Y., Feng, H.L., Ma, J.M., Zhang, Z.Y., Lu, J.X., Chen, Y.S., Yang, S.E. and Gu, J.H., 2010. Analysis of the dielectric constants of the Ag<sub>2</sub>O film by spectroscopic ellipsometry and single-oscillator model. *Physica B: Condensed Matter*, 405(7),1922-1926.
17. Girija, K.G., Somasundaram, K., Debnath, A.K., Topkar, A. and Vatsa, R.K., 2018. Enhanced H<sub>2</sub>S sensing properties of Gallium doped ZnO nanocrystalline films as investigated by DC conductivity and impedance spectroscopy. *Materials Chemistry and Physics*, 214, 297-305.
18. Govor, L. V., Reiter, G., & Parisi, J. (2016). When hole extraction determines charge transfer across metal-organic-metal structure. *EPL (Europhysics Letters)*, 113(5), 57002.
19. Hasbullah, N. F., David, J. P. R., & Mowbray, D. J. (2011). Dark current mechanisms in quantum dot laser structures. *Journal of Applied Physics*, 109(11), 113111.
20. Ismail, R.A., Yahya, K.Z. and Abdulrazaq, O.A., 2005. Preparation and photovoltaic properties of Ag<sub>2</sub>O/Si isotype heterojunction. *Surface Review and Letters*, 12(02), 299-303.
21. Jo, M., Park, H., Lee, J. m., Chang, M., Jung, H. S., Lee, J. H., & Hwang, H. (2008). Effect of Oxygen Postdeposition Annealing on Bias Temperature Instability of Hafnium Silicate MOSFET. *IEEE Electron Device Letters*, 29(4), 399-401.

22. Khusayfan, N. M., Qasrawi, A. F., Alharbi, S. R., Khanfar, H. K., & Kayed, T. S. (2021). Band offsets, dielectric dispersion and some applications of CdSe/GeO<sub>2</sub> heterojunctions. *Optik*, 231, 166506.
23. Khusayfan, N. M., Qasrawi, A. F., & Khanfar, H. K. (2018a). Design and characterization of Au/In<sub>4</sub>Se<sub>3</sub>/Ga<sub>2</sub>S<sub>3</sub>/C field effect transistors. *Results in Physics*, 8, 1239-1244.
24. Khusayfan, N.M., Qasrawi, A.F. and Khanfar, H.K., 2018. Design and electrical performance of CdS/Sb<sub>2</sub>Te<sub>3</sub> tunneling heterojunction devices. *Materials Research Express*, 5(2), 026303.
25. Kim, H., Jin, C., Park, S., Kwon, Y., Lee, S. and Lee, C., 2012. Influence of ZnO encapsulation on the luminescence property of GeO<sub>2</sub> nanowires. *Physica Scripta*, 2012(T149), 014052.
26. Kim, H.W., Na, H.G., Kwak, D.S., Cho, H.Y. and Kwon, Y.J., 2013. Enhanced gas sensing characteristics of Ag<sub>2</sub>O-functionalized networked In<sub>2</sub>O<sub>3</sub> nanowires. *Japanese Journal of Applied Physics*, 52(10S), p.10MD01.
27. Li, Q., Xu, M., Fan, H., Wang, H., Peng, B., Long, C., & Zhai, Y. (2013). Dielectric properties investigation of Cu<sub>2</sub>O/ZnO heterojunction thin films by electrodeposition. *Materials Science and Engineering: B*, 178(8), 496-501.
28. Lu, C., Lee, C. H., Zhang, W., Nishimura, T., Nagashio, K., & Toriumi, A. (2014). Structural and thermodynamic consideration of metal oxide doped GeO<sub>2</sub> for gate stack formation on germanium. *Journal of Applied Physics*, 116(17), 174103.
29. Madelung, O. (2012). *Semiconductors: Data Handbook* (3 ed.): Springer Berlin Heidelberg.
30. Miao, M.-S., Yarbrow, S., Barton, P. T., & Seshadri, R. (2014). Electron affinities and ionization energies of Cu and Ag delafossite compounds: A hybrid functional study. *Physical Review B*, 89(4), 045306.
31. Ndikilar, C. E., Taura, L., Ejuh, G., & Muhammad, A. (2018). RHF and DFT Study of the Molecular and Electronic Properties of (SiO<sub>2</sub>)<sub>n</sub> and (GeO<sub>2</sub>)<sub>n</sub> Nanoclusters. *Modern Applied Science*, 12(9), 108-118.
32. Pan, Y., Pu, D. and Jia, Y., 2020. Adjusting the correlation between the oxidation resistance and mechanical properties of Pt-based thermal barrier coating. *Vacuum*, 172, 109067.



33. Panto, F., Fan, Y., Stelitano, S., Fazio, E., Patanè, S., Frontera, P., Antonucci, P., Pinna, N. and Santangelo, S., 2017. Electrospun C/GeO<sub>2</sub> paper-like electrodes for flexible Li-ion batteries. *International Journal of Hydrogen Energy*, 42(46), 28102-28112.
34. Pintilie, L., Stancu, V., Trupina, L., & Pintilie, I. (2010). Ferroelectric Schottky diode behavior from a SrRuO<sub>3</sub>Pb(Zr<sub>0.2</sub>Ti<sub>0.8</sub>) O<sub>3</sub>-Ta structure. *Physical Review B*, 82(8), 085319.
35. Pozar, D. M. (2011). *Microwave engineering*: John wiley & sons.
36. Qasrawi, A. F. (2014). Electrical parameters of Al/InSe/C RF sensors. *Physica Scripta*, 89(6), 065802.
37. Qasrawi, A. F., & Aloushi, H. D. (2019). Formation, negative capacitance and negative conductance effects in Selenium stacked layers sandwiched with Ag nanosheets. *Materials Research Express*, 6(8), 086435.
38. Qasrawi, A. F., & Khanfar, H. K. (2020). Al/MoO<sub>3</sub>/ZnPc/Al Broken Gap Tunneling Hybrid Devices Design for IR Laser Sensing and Microwave Filtering. *IEEE Sensors Journal*, 20(24), 14772-14779.
39. Roh, H.B., Seo, J.H., Yoon, Y.J., Bae, J.H., Cho, E.S., Lee, J.H., Cho, S. and Kang, I.M., 2014. Evaluation of Radio-Frequency Performance of Gate-All-Around Ge/GaAs Heterojunction Tunneling Field-Effect Transistor with Hetero-Gate-Dielectric by Mixed-Mode Simulation. *Journal of Electrical Engineering and Technology*, 9(6), pp.2070-2078.
40. Shi, S., Cho, S., Goto, T., & Sekino, T. (2020). The effects of sintering temperature on mechanical and electrical properties of Al<sub>2</sub>O<sub>3</sub>/Ti composites. *Materials Today Communications*, 25, 101522.
41. Sulaiman, N., Taura, L., Abdullahi Lawal, G. A., & Musa, A. (2019). Solvent Effects on the Structural, Electronic, Non-Linear Optical and Thermodynamic Properties of Perylene Based on Density Functional Theory. *JMSRR*, 3(3), 1-13.
42. Sze, S. M., & Ng, K. K. (2006). *Physics of Semiconductor Devices* (3 ed.). New Jersey: Wiley.
43. Taya, S.A. and El-Agez, T.M., 2011. Ellipsometry of anisotropic materials: a new efficient polynomial approach. *Optik*, 122(8), pp.666-670.
44. Tsukada, I., Koide, N., Sasago, Y. and Uchinokura, K., 1998. Surface flatness and structure of the bc-cleaved plane of spin-Peierls material CuGeO<sub>3</sub>. *Physical Review B*, 57(19), p.11927.

45. Wang, S., Hu, J., Jiang, L., Li, X., Cao, J., Wang, Q., Wang, A., Li, X., Qu, L. and Lu, Y., 2019. High-performance 3D CuO/Cu flowers supercapacitor electrodes by femtosecond laser enhanced electrochemical anodization. *Electrochimica Acta*, 293, pp.273-282.
46. Wu, F., Xia, H., Sun, H., Zhang, J., Gong, F., Wang, Z., Chen, L., Wang, P., Long, M., Wu, X. and Wang, J., 2019. AsP/InSe van der Waals tunneling heterojunctions with ultrahigh reverse rectification ratio and high photosensitivity. *Advanced Functional Materials*, 29(12), p.1900314.
47. Yan, S., Song, H., Lin, S., Wu, H., Shi, Y., & Yao, J. (2019). GeO<sub>2</sub> Encapsulated Ge Nanostructure with Enhanced Lithium-Storage Properties. *Advanced Functional Materials*, 29(8), 1807946.
48. Yamamoto, K., Ueno, R., Yamanaka, T., Hirayama, K., Yang, H., Wang, D. and Nakashima, H., 2011. High-performance Ge metal-oxide-semiconductor field-effect transistors with a gate stack fabricated by ultrathin SiO<sub>2</sub>/GeO<sub>2</sub> bilayer passivation. *Applied physics express*, 4(5), p.051301.
49. Zhou, J., Han, G., Xu, N., Li, J., Peng, Y., Liu, Y., Zhang, J., Sun, Q.Q., Zhang, D.W. and Hao, Y., 2019. Experimental validation of depolarization field produced voltage gains in negative capacitance field-effect transistors. *IEEE Transactions on Electron Devices*, 66(10), pp.4419-4424.

## تأثير سماكة الصفائح النانوية لأكسيد الفضة على أداء الأجهزة متعددة الوظائف (المنيوم /

### أكسيد الجرمانيوم /أكسيد الفضة / أكسيد الجرمانيوم / الكربون)

عاطف قسراوي<sup>1</sup>، حازم خنفر<sup>2</sup>

<sup>1</sup>قسم الفيزياء، الجامعة العربية الأمريكية، فلسطين

atef.qasrawi@aaup.edu

<sup>2</sup>قسم هندسة الاتصالات، الجامعة العربية الأمريكية، فلسطين

hazem.khanfar@aaup.edu

#### ملخص

في هذه الدراسة تم استخدام طبقات مكندسة من أكسيد الجرمانيوم تشتمل على صفائح نانوية من أكسيد الفضة لتصنيع الأجهزة الإلكترونية متعددة الوظائف. تم تسجيل تأثير الصفائح النانوية المصنعة من أكسيد الفضة على الأداء الإلكتروني للطبقات المكندسة من أكسيد الجرمانيوم. خضعت الطبقات الثلاث وهي أكسيد الجرمانيوم /أكسيد الفضة / أكسيد الجرمانيوم والمتكاثفة على رقائق الالمنيوم تحت ضغط تغريغ  $10^{-5}$  ملي بار لقياسات حيود الأشعة السينية، والإلكترون الضوئي للأشعة السينية، وتقنيه طيف الأشعة السينية الصادرة من الالكترونات الضوئية، والمقاومة التحليل الطيفي، والسعة، وتقنيات خصائص الجهد والتيار. اثبتت تحليلات طيف المقاومة ان التغير في سمك طبقة أكسيد الفضة في نطاق 25-75 نانومتر يمكن أن ينجح في هندسة نطاقات تشغيل أجهزة أكسيد الجرمانيوم /أكسيد الفضة / أكسيد الجرمانيوم عند تشغيلها كمرشحات تمرير / رفض النطاق في مجال التردد من 0.01 إلى 1.80 جيجا هرتز، حيث إنها تُظهر وجود ثلاثة خطوط مرور بالقرب من 1.0 جيجا هرتز وفوقها. بالإضافة إلى ذلك، لوحظ تأثير سعة سالب يمكن التحكم فيه مصحوبًا بظاهرة الرنين والرنين المضاد في مجالات التردد المدروسة. من ناحية أخرى، كشفت الدراسات التي أجريت على خصائص السعة والجهد عن امتلاك هذه الرقائق خصائص الترانزستورات الرقيقة.

الكلمات الدالة: رقائقي، أكسيد الفضة، أكسيد الجرمانيوم، مرشح، ترانزستور